Characterization of Ni thin films following thermal oxidation in air

Luis De Los Santos Valladares,[a] Adrian Ionescu, Stuart Holmes, and Crispin H. W. Barnes
Cavendish Laboratory, Department of Physics, University of Cambridge, J.J Thomson Ave., Cambridge CB3 0HE, United Kingdom

Angel Bustamante Domínguez, Oswaldo Avalos Quispe, and Juan C. González
Laboratorio de Cerámicos y Nanomateriales, Facultad de Ciencias Físicas, Universidad Nacional Mayor de San Marcos, Ap. Postal 14-0149, Lima, Peru

Silvia Milana, Matteo Barbone, and Andrea C. Ferrari
Cambridge Graphene Centre, University of Cambridge, 9 J.J. Thomson Avenue, Cambridge CB3 0FA, United Kingdom

Henry Ramos
National Institute of Physics, College of Science, University of the Philippines, Diliman, Quenzon City 1101, Philippines

Yutaka Majima
Materials and Structures Laboratory, Tokyo Institute of Technology, 4259 Nagatsuta cho, Midori ku, Yokohama 226-8503, Japan

(Received 30 May 2014; accepted 5 September 2014; published 22 September 2014)

The authors study the thermal oxidation of nickel thin films (50 nm) fabricated by conventional thermal evaporation, resulting from annealing in air at 300, 325, 350, 400, and 700 °C. The characterization is performed by x-ray diffraction, Raman spectroscopy, superconducting quantum interference device magnetometry, and scanning electron microscopy. These techniques show that the oxidation increases with annealing temperature. The formation of granular films of coexisting Ni and NiO is confirmed after annealing at 400 °C. The magnetic measurements indicate coexisting ferromagnetism and antiferromagnetism, corresponding to Ni and NiO contributions. The magnetic hysteresis loops reveal exchange bias in the samples annealed at 235, 350, and 400 °C due to the competition between the exchange interactions at the Ni/NiO interfaces. © *2014 American Vacuum Society*. [http://dx.doi.org/10.1116/1.4895846]

I. INTRODUCTION

Nickel is a ferromagnetic transition metal with a Curie temperature $T_C = 630$ K (magnetic moment $\mu \approx 0.6\,\mu_B$/atom).[1] Its magnetization derives from the spin polarization of the 3*d* electrons, which are very sensitive to the local environment.[2] Its magnetic properties, together with its low electrical resistivity [6.84 $\mu\Omega$ cm (Ref. 1)], and its high resistance to oxidation,[3,4] make it useful in several applications, such as for the metallization of ferrites, as a corrosion–resistant coating, as an absorber in solar to thermal energy conversion and in high density recording, see for example, Refs. 5–7.

Ni oxidizes to chemically stable NiO, which has a cubic NaCl-type structure.[1] At room temperature (RT), "pure" (without contaminants, doping, and/or imperfections) $Ni^{2+}O^{2-}$ is an insulator with high resistivity [$\rho \approx 10^{11}$ Ω/m at 50 °C (Ref. 8)] and behaves antiferromagnetically below the Néel temperature $T_N = 523$ K.[9,10] However, NiO becomes a *p*-type semiconductor, with tuneable band gap ~4.0–4.3 eV, when its stoichiometry is altered by the presence of Ni vacancies and/or interstitial oxygen in the NiO crystal.[11,12] For example, by doping NiO with monovalent atoms (such as Li^+), the amount of Ni^{3+} increases, resulting in a decrease of resistivity[10,13,14] and an increase of the dielectric constant.[15] Thin films of NiO are attractive for applications as antiferromagnetic layers in spin-valve heterostructures,[16] gas sensors,[17] *p*-type transparent conducting electrodes,[14,18] thermoelectric devices,[19] and in electrochromic display devices.[20,21] Furthermore, we have recently shown that the appearance of a ferromagnetic moment on nominally antiferromagnetic NiO nanoparticles can be attributed to a disordered shell (surface) possessing a significant polarizable magnetization.[22]

The oxidation of nickel thin films, as well as the direct deposition of NiO films onto a target substrate, have been intensively investigated by magnetron sputtering,[14,20,21,23,24] thermal evaporation,[25,26] electro-deposition,[27] chemical vapor deposition,[9,28] reactive chemical ion beam deposition,[29] and sol–gel deposition.[30] However, in most of these techniques, it is difficult to control the amount of oxidation. Thermal oxidation has proven to be an easy *ex situ* technique to obtain metal oxide films and to improve metal crystallization.[31–33] This consists in annealing metal surfaces at high temperatures in air flow or in oxygen atmosphere to obtain the partial (or complete, as desired) oxidation of the metal films.

There are a few reports on oxidation evolution or its effects on the properties of nickel films. These consider Ni oxidation in oxygen atmosphere at high T (between 900 and 1400 °C)[3,4] or at 500 °C.[26] There is however, to the best of our knowledge, no report on the oxidation process of Ni thin films at lower T and in air, nor its effects on the physical properties, such as magnetism. Here, we study the phase

[a]Electronic addresses: ld301@cam.ac.uk; luisitodv@yahoo.es

formation and the effect of thermal oxidation on morphology and magnetic properties in polycrystalline Ni thin films. We find that their thermal oxidation depends on the annealing temperature (AT) and annealing promotes the formation of granular films. Our results demonstrate that the magnetic properties of nickel thin films depend on the morphology, and crystallization of the oxide formed on it.

II. EXPERIMENT

Ni is evaporated on polished Si/SiO_2 substrates using an EDWARDS 306 evaporator. Si/SiO_2 is used as a substrate in order to avoid adhesion promoters, such as chromium or titanium, and to prevent the formation of metal alloys during annealing. The substrates (2 mm thick) are cut into $1 \times 2\,cm^2$ pieces, cleaned with acetone, isopropyl alcohol and ultrasound bathed for 10 min. Small Ni pellets (99.999% purity) are then evaporated from an alumina coated crucible at 10^{-5} Pa pressure. The deposition rate is maintained at 0.1 nm/s, and the Ni thickness is measured by a quartz crystal microbalance, located 10 cm above the source and next to the substrates. During deposition, the substrates are maintained at RT in order to characterize only post-thermal oxide formation. The as-deposited samples consist of Ni (50 nm thickness) on Si/SiO_2.

Thermal oxidation is carried out by annealing the as-deposited samples in a tubular oven (LENTON LTF–PTF Model 16/610) in air, similar to Refs. 31–33. Here, the samples are annealed at 300, 325, 350, 400, and 700 °C, with a heating rate ~2 °C/min. Once the desired maximum T is reached, it is maintained for 3 h to allow oxidation and free diffusion of Ni atoms on the surface. The quenching rate is set to 2.5 °C/min, so as to minimize the stress induced in the films.

Phase formation and surface crystallization are analyzed by x-ray diffraction (XRD) using a universal diffractometer Bruker AXS D8 model FOCUS ($Cu–K\alpha_1$ radiation). The step size is 0.02° per sec (2θ). The average sizes of the crystallites are estimated from the main reflections of the XRD scans using the Scherrer equation[34] and neglecting peak broadening induced by residual stresses[34]

$$D = \frac{0.916\,\lambda}{\beta_{hkl}\cos\theta_{hkl}}, \tag{1}$$

where D is the average crystallite size, λ is the wavelength of the applied x-ray beam ($\lambda_{Cu–K\alpha1} = 0.154056$ nm), θ_{hkl} is the Bragg angle, and β_{hkl} is the diffraction line broadening (in radians), which can be determined by measuring the full width at half maximum (FWHM) of the principal (hkl) reflections for each phase.

Raman spectra are acquired at 458 nm using a Renishaw InVia micro-Raman spectrometer, in backscattering at RT, using an optical microscope equipped with 100× objective, corresponding to a laser spot ~1 μm, and 2400 lines/mm grating. The power on the sample is kept below 100 μW to avoid possible heating effects. The surface morphology is analyzed by scanning electron microscopy (SEM) and atomic force microscopy (AFM). The SEM micrographs are obtained in a Philips XL-30, with acceleration voltages of 5 and 10 kV. Before SEM analysis, the surfaces are scratched with the help of a needle in order to reveal parts of the SiO_2 substrate, and hence better distinguish the Ni films. We use a Nanoscope Dimension 3100 (Digital Instruments) AFM in tapping mode.

The magnetic measurements are performed in a DC magnetic property measurement system superconducting quantum interference device (DC-MPMS-SQUID) from Quantum Design. The samples are cut into rectangles with side dimensions a and c (thickness $b = 50$ nm) as listed in Table I. The data are collected under different magnetic fields, in the interval of −5 to 5 kOe and at 50 K, which are applied in plane (parallel to c) and perpendicular to the substrates (parallel to b). The data are corrected by removing the diamagnetic contribution of the sample holder and the substrate. Further corrections include the subtraction of the demagnetizing field (H_D)[35]

$$H_D = -N_D M, \tag{2}$$

where M is the magnetization and N_D is the demagnetizing factor (which depends mainly on the geometry of the sample and the direction of the applied field). For thin films, the parallel and perpendicular demagnetization factors were reported to be close to 0 and 1, respectively.[36] We calculate them nonetheless by using the Aharoni technique,[37,38] as listed in Table I.

III. RESULTS AND DISCUSSIONS

Figure 1 shows the XRD scans of the samples before and after annealing. No nickel silicide is detected by XRD, which means that the film does not react with the substrate during deposition or annealing. Following deposition, the sample shows two main diffraction peaks at ~44.6° and 52.1° corresponding to the (111) and (200) Miller indices of Ni (PDF-2 card 270–989,[39] cubic structure $Fm\bar{3}m$). This implies that, during deposition, the Ni atoms reach the substrate with enough thermal energy to form a mainly (111) textured Ni crystalline layer. Despite Ni being oxidized in contact with air, no oxide peaks are detected by XRD. Annealing at 300 and 325 °C for 3 h improves the crystallite orientation along the (111) and (200) planes, which is reflected in the sharpened peaks. Following annealing at higher T, oxide formation is detected. At 350 °C, two small peaks around $2\theta = 37.4°$ and 43.2°, corresponding to the

TABLE I. Lateral dimensions of the annealed Ni thin films and demagnetizing factors along the different directions of the externally applied magnetic field.

Annealed sample (°C)	a (mm)	c (mm)	Area (mm^2)	$N_c \times 10^{-5}$	$N_b \times 10^{-3}$
300	3.45 ± 0.1	3.76 ± 0.1	12.97 ± 0.7	2.66	999.94
325	2.52 ± 0.1	3.46 ± 0.1	8.72 ± 0.6	2.84	999.93
350	3.12 ± 0.1	4.31 ± 0.1	13.45 ± 0.7	2.32	999.94
400	3.53 ± 0.1	3.85 ± 0.1	13.59 ± 0.7	2.60	999.95
700	3.64 ± 0.1	4.54 ± 0.1	16.53 ± 0.8	2.22	999.95

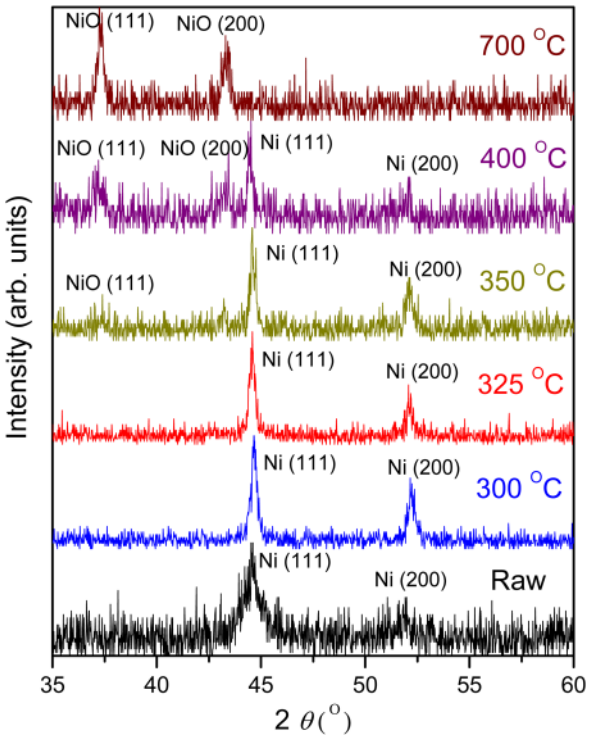

FIG. 1. (Color online) X-ray diffractograms of Ni thin films annealed at different T for 3 h in air.

Miller indexes (111) and (200) of NiO (PDF-2 card 47–1049,[39] cubic structure $Fm\bar{3}m$) appear. This indicates that, together with crystallization improvement, annealing at this T promotes some Ni-O bonding. At 400 °C, the height of the NiO peaks grows, whereas those of Ni decrease. Upon annealing at higher T, such as 700 °C, complete oxidation is obtained.

Note that the intensity of the (111) NiO peak is higher than the (200), indicating that the NiO films grow preferentially textured along the (111) direction rather than along the (200). A similar result was reported in Ref. 26 after thermally oxidizing an evaporated Ni thin film at 500 °C, although they did not provide structural information on the Ni film prior to the oxidation. In contrast, in the case of randomly dispersed NiO nanoparticles[40] and nanowires,[41] the x-ray intensity is higher for the (200) diffraction peak as would be expected from powder diffraction.[39] This is also the case when NiO is directly deposited on amorphous glass substrates.[21,28,30,42] However, in our case, the oxide layer is not directly deposited on an amorphous substrate, but it grows on the annealed, (111) textured Ni film. It was reported by Ref. 43, by means of ion scattering and reflection high energy electron diffraction, that NiO (111) grows epitaxially on Ni (111) surfaces. Because of the large lattice mismatch (19%) between the two surfaces, it was proposed that the NiO initially takes a precursor state of an octopolar structure with a significant distortion. The oxidation mechanism is discussed below in more detail.

Table II lists the XRD (*hkl*) indices, angle positions, and mean crystallite sizes. As discussed above, the XRD diffraction intensities increase sharply as the AT increases. For example, at 300 °C, the diffraction FWHM is large compared to 350 °C. This indicates that the improvement of the crystallization is due to the growth of Ni crystallites. From this table, the mean crystallite size of the pristine Ni sample is ~8 ± 2 nm, increasing to ~36 ± 2 nm at 400 °C. However, it is hard to determine the size of the NiO crystallites due to the noisy background. A rough estimation by the Scherrer equation[34] yields ~20 ± 3 nm after annealing at 400 °C, increasing to ~25 ± 2 nm at 700 °C. Table II also lists the surface roughness R_{RMS} (root mean square) obtained by AFM after scanning areas of 20 μm^2 on each sample. Notably, the roughness of the surface increases with T. This is due to the transformation of the Ni film into a granular NiO film as explained in more detail below.

TABLE II. Phase formation, Miller indices (*hkl*), angle positions and mean crystallite sizes as obtained from the principal peaks of the XRD scans. R_{RMS}: Roughness (root mean square) obtained by AFM over areas of 20 μm^2.

Annealing temperature (°C)	R_{RMS}	Phase	(*hkl*)	2θ (°)	Crystallite size (nm)
As-grown	8.2	Ni	(111)	44.60	8 ± 2
			(200)	51.98	8 ± 2
300	10.5	Ni	(111)	44.66	34 ± 2
			(200)	52.16	34 ± 2
325	17.5	Ni	(111)	44.58	34 ± 2
			(200)	52.08	34 ± 2
350	20.6	Ni	(111)	44.58	36 ± 2
			(200)	52.12	36 ± 2
		NiO	(111)	37.40	—
			(200)	43.20	—
400	30.8	Ni	(111)	44.52	36 ± 2
			(200)	52.12	—
		NiO	(111)	37.4	20 ± 3
			(200)	43.2	—
700	32.3	NiO	(111)	37.4	25 ± 2
			(200)	43.2	—

Figure 2 presents the Raman spectra of the Ni films annealed at different T. Figure 2(a) shows representative spectra and a reference spectrum for the Si/SiO_2 substrate. The peak at 521 cm^{-1} is the first-order Raman peak of Si, whereas the weaker features at ~300, 433, 620, 670, and 825 cm^{-1}, as well as the more prominent band at ~1100 cm^{-1}, are due to higher-order Raman scattering processes.[44] The Raman spectra of annealed films and reference Si/SiO_2 substrate are acquired using identical exposure time and incident laser power. After normalizing the intensity of the first order Si peak in the Si/SiO_2 reference spectrum to the Si intensity in the spectra of the annealed Ni films, a point-to-point subtraction of the normalized reference spectrum from the annealed Ni films spectra is implemented, Fig. 2(b). For all the samples, we observe Raman bands from NiO in the spectral region above 400 cm^{-1}. The Raman peaks below 1200 cm^{-1} in Fig. 2(b) are due to first- and second-order Raman scattering by phonons in NiO,[45,46] whereas the band above 1200 cm^{-1} originates from scattering by two magnons in NiO.[45,46] Magnons are quantized excitations of electron spin waves occurring in magnetically

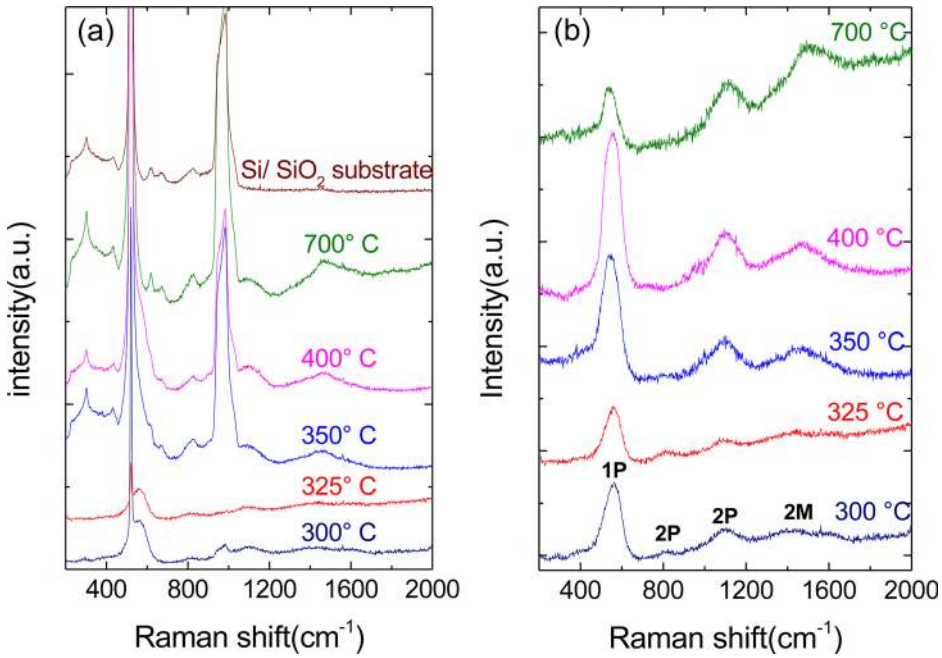

FIG. 2. (Color online) (a) Representative Raman spectra for different AT and of a reference Si/SiO_2 substrate. (b) Raman spectra after subtraction of the Si/SiO_2 spectrum.

ordered materials.[47] Inelastic light scattering with magnons can occur in magnetic materials due to spin-orbit coupling.[47] Scattering by two magnons happens when the incoming laser causes an excitation of pairs of spin fluctuations[47,48] and subsequently the excited charges return to the ground orbital[48] emitting a scattered phonon.[48]

The band at $\sim 570\,cm^{-1}$ is assigned to the first-order one-phonon (1P) LO mode of NiO, whereas the bands at ~ 730 and $\sim 1090\,cm^{-1}$ correspond to second-order two-phonon (2P) modes, respectively, 2TO and 2LO.[45,46] According to group analysis,[46] the observed first-order Raman band derives from symmetry-breaking imperfections such as defects, i.e., Ni vacancies, or disorder in the crystal lattice, therefore its FWHM can be used as an indication of presence of defects in the NiO samples.[49]

The band at $\sim 1490\,cm^{-1}$ is attributed to two-magnon (2M) scattering[45,46] and can be used, in combination with the first-order Raman band, to monitor the amount of defects-induced disorder, since its FWHM experiences a broadening in presence of disorder or substitutional defects.[49]

The Raman spectra confirm the presence of NiO for all the AT, although, using XRD, NiO could be detected only after annealing to 350 °C (see Fig. 1). As discussed more in detail below, the NiO growth starts from the surface of the Ni film and increases both laterally and in depth, as Ni is consumed, consistent with our Raman data detecting NiO already at 300 and 325 °C, where the contribution of NiO arises predominantly from the surface, and cannot be detected by XRD.

The intensity ratio between the first-order one-phonon (1P) band at $\sim 570\,cm^{-1}$ and the second order two-phonon (2P) band $\sim 1090\,cm^{-1}$, I(1P)/I(2P), decreases with increasing AT. This is similar to what is reported for nanosized NiO particles,[50] where I(1P)/I(2P) was found to decrease with increasing nanoparticle size. This suggests that in our samples the NiO grains grow with increasing annealing temperature.

The FWHM of both 1P and 2M bands do not experience any significant broadening as a function of T, indicating that the treatment does not induce any degradation of the quality of the resulting NiO and that crystallinity is preserved, as also seen by XRD.

The oxidation kinetics depends on many factors, such as T, oxygen partial pressure, annealing time, etc. Hence, it cannot be resolved solely by the techniques used here. Here, annealing is performed in air, thus the oxygen partial pressure can be considered constant (atmospheric pressure). Note that oxidation starts immediately after evaporation, as a slow and natural process, due to the exposure of Ni to air. This was previously confirmed in Ref. 51 by Auger electron spectroscopy and contact resistance measurements of nickel films exposed to a typical laboratory air environment. In Ref. 51, the limiting oxide thickness did not exceed 10 Å.

A possible oxidation mechanism is schematically represented in Fig. 3. Similarly to the oxidation of common metals,[52,53] the oxidation of Ni should occur by transfer of electrons through the interface to form a monolayer of adsorbed oxygen ions at the surface, together with the diffusion of oxygen anions into the metal film.[52,53] The oxygen anions are initially absorbed to form a thin oxide layer on the Ni surface, Fig. 3(a). During the initial stages of annealing, the Ni atoms redistribute to preferred sites and interact with the atmosphere. In addition, nucleation sites appear for NiO on the surface and they expand laterally [see Fig. 3(b)]. The preferred nucleation sites are structural defects, such as grain boundaries, dislocations, impurities, or dust particles. The oxide islands grow rapidly to form a NiO film partially

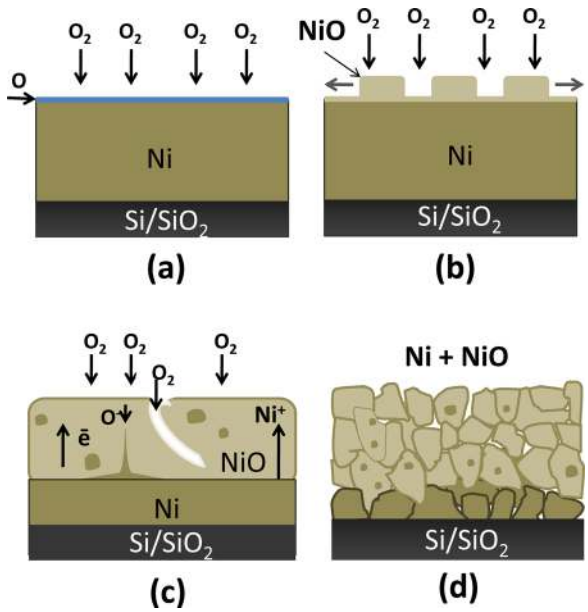

FIG. 3. (Color online) Schematic representation of the thermal oxidation process of a nickel film. The oxidation occurs by transfer of electrons, nickel cations, and oxygen anions through the film. Annealing controls the oxidation process and the morphology of the film.

protecting the Ni surface from air. Annealing above 350 °C accelerates the growth of the oxide film by diffusion of Ni cations into this NiO layer. The reaction can be thermally controlled such that

$$\mathrm{Ni} + 1/2\mathrm{O}_2 \xrightarrow{\Delta} \mathrm{NiO}. \tag{3}$$

In addition, oxygen may penetrate the NiO layer through cracks and microchannels, which can be promoted by metal diffusion at higher T [Fig. 3(c)]. However, if we assume that the Ni^+ cations located at the Ni/NiO interface diffuse (through imperfection sites or grain boundaries[54]) faster than the O^- anions, then they could reach the oxygen atoms first. Thus, additional NiO forms, which is incorporated into the oxide network, and results in an increase of the thickness of the oxide layer. The oxidation rate decreases as the thickness of the oxide layer increases and the amount of Ni^+ ions in the buffer layer decreases. Nevertheless, as shown here, the oxidation rate also depends on the AT. For example, the coexistence of Ni and NiO phases is detected at 400 °C as discussed in the XRD analysis above. Thermal oxidation also affects the morphology of the film making it granular, as it is discussed below. Depending on AT, partial or complete oxidation of the films can be obtained [Fig. 3(d)]. Therefore, in our conditions, the complete oxidation of the Ni films occurs at high T, such as 700 °C.

SEM images of Ni films on Si/SiO_2 substrates after annealing at 300, 325, 350, 400, and 700 °C are shown in Fig. 4. As mentioned in Sec. II, some are scratched with a needle in order to reveal the SiO_2 surface and to contrast it to the Ni film. After annealing at 300 °C a rough surface covers the substrate, together with some small holes formed due to Ni diffusion. After annealing at 325 °C the pores increase in size but decrease in density. This implies that the Ni diffusion is promoted by the increase in AT. The sample annealed at 350 °C shows a rough and porous surface with an area of uncovered SiO_2, see Fig. 4. Peeled parts of the oxide film reveal a bottom layer consisting of almost unreacted Ni. The roughness of the Ni bottom layer is smaller compared to the outside surface, indicating that the oxidation takes place from the surface to the bottom part of the film, as expected.[53] The AFM image in Fig. 4 reveals the formation of nanoparticles. However, it is not clear if they are made of pure NiO or a mixture of NiO and Ni. Annealing at 400 °C increases the grain size; this is accompanied by porosity and crack formation. These characteristics are generally observed in amorphous materials,[55]

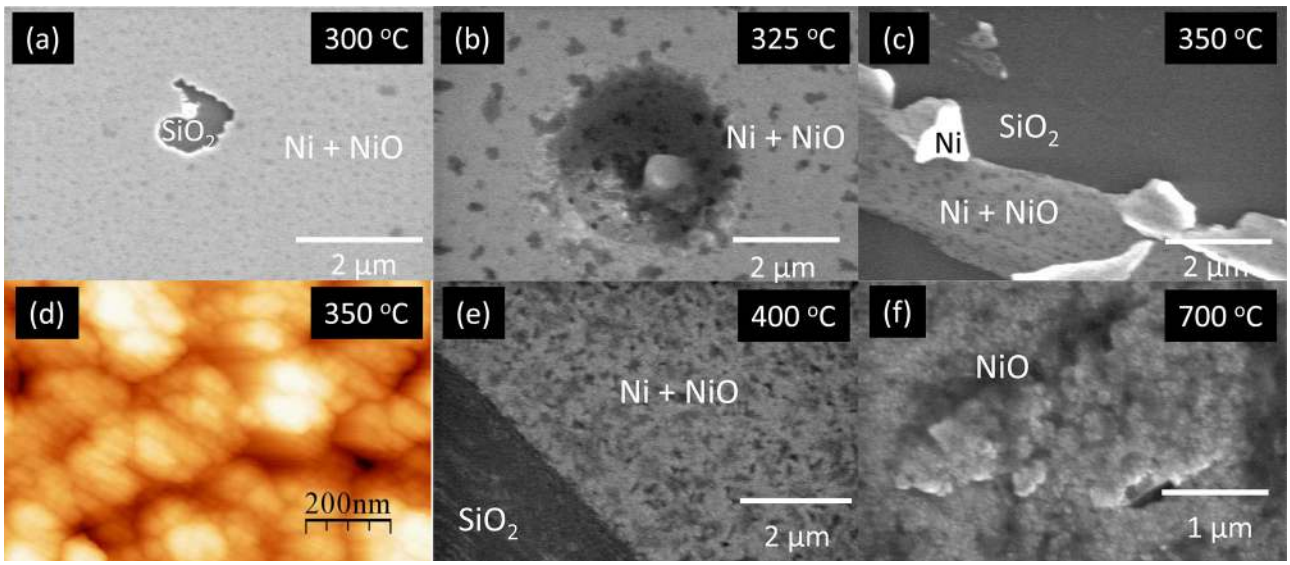

FIG. 4. (Color online) (a)–(f) Micrographs of nickel films on Si/SiO_2 substrates at different ATs. (d) AFM image of the surface of the sample annealed at 350 °C shown in (c).

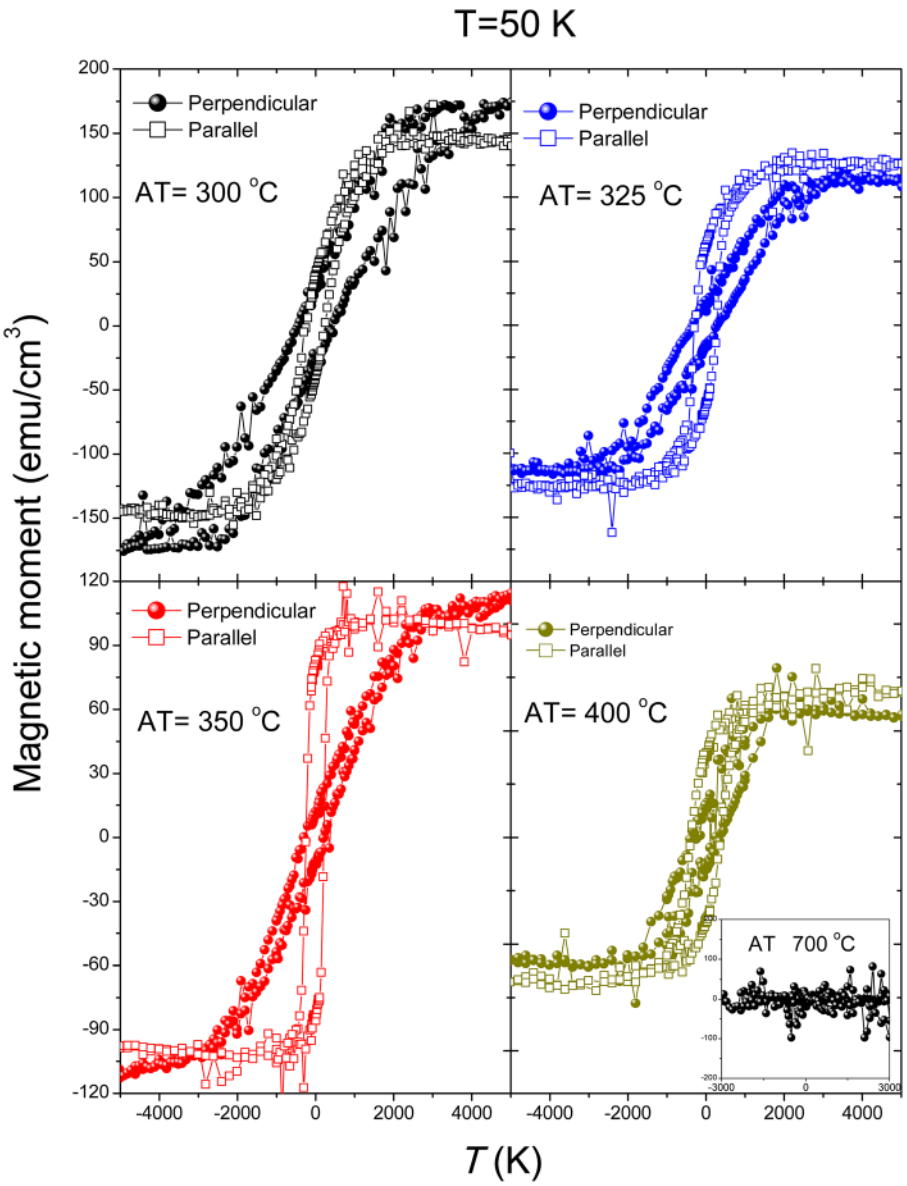

FIG. 5. (Color online) Magnetic hysteresis loops at 50 K for different ATs.

though some degree of crystallinity persists in our films as seen by XRD. After annealing at 700 °C, the sample consists of a film of NiO grains with a rough top surface. With increasing AT the adhesion to the substrate becomes poorer and the films start to exfoliate. This effect should be related to the large difference between the heat capacities of the Ni film [444 J kg^{-1} K^{-1} (Ref. 1)] and the SiO_2 substrate [725 J kg^{-1} K^{-1} (Ref. 56)].

Figure 5 reports the *M(H)* dependence of the samples measured parallel (in-plane) and perpendicular (out-of-plane) to the films at 50 K. The hysteresis loops identify the presence of ferromagnetic Ni domains.[35] Note that the in-plane loops reach saturation easier than those obtained with the out-of-plane applied field, revealing that the preferred direction of the magnetization is in-plane.[35]

The magnetic characteristics obtained from the hysteresis loops are summarized in Table III. According to the data, the saturation magnetization (M_S) and the saturation field (H_S) decrease as AT increases. This behavior is caused by the decrease in the amount of pure Ni as it is consumed in the oxidation process, mediated by the AT, and the amount of NiO, containing antiferromagnetic domains, increases, requiring a higher external field to saturate. On the other hand, the remnant magnetization (M_R) increases initially with AT, when measured in-plane. This trend is not followed for the sample annealed at 400 °C, which contain fewer ferromagnetic ordered spins due to the higher amount of NiO. Similarly, the M_R/M_S ratio detected when the applied field is in-plane increases with AT. This is related to the presence of the antiferromagnetic[35] NiO, which hinders the reorientation of the ferromagnetic moments of the Ni films by exchange bias interaction,[57] which in turn contributes to the increase of the remanence and coercive field. As mentioned above, the sample annealed at 350 °C has the largest Ni crystallites,

TABLE III. Measured values of the saturation magnetization (M_S), remanent magnetization (M_R), saturation field (H_S), and coercive fields (H_C) extracted from the magnetic measurements (at 50 K) of nickel thin films following annealing at 300, 325, 350, and 400 °C.

$T_{Annealing}$ (°C)	Direction	M_S (emu/cm^3)	M_R (emu/cm^3)	M_R/M_S	H_S (Oe)	$H_{C(+)}$ (Oe)	$H_{C(-)}$ (Oe)	$\lvert H_{C(+)}\rvert - \lvert H_{C(-)}\rvert$ (Oe)
300	Parallel	355 ± 62	95 ± 16	0.27 ± 0.09	2000 ± 10	230 ± 5	−230 ± 5	0 ± 10
	Perpendicular	300 ± 52	74 ± 13	0.24 ± 0.08	4000 ± 10	380 ± 5	−395 ± 5	15 ± 10
325	Parallel	270 ± 30	140 ± 10	0.52 ± 0.09	1900 ± 10	282 ± 5	−300 ± 5	−18 ± 10
	Perpendicular	255 ± 15	38 ± 8	0.14 ± 0.04	3000 ± 10	196 ± 5	−290 ± 5	−94 ± 10
350	Parallel	214 ± 8	170 ± 6	0.80 ± 0.06	1600 ± 5	217 ± 5	−253 ± 5	−36 ± 10
	Perpendicular	190 ± 10	24 ± 8	0.13 ± 0.05	3000 ± 10	303 ± 10	−262 ± 10	−41 ± 20
400	Parallel	110 ± 10	68 ± 4	0.61 ± 0.09	1600 ± 5	403 ± 5	−439 ± 5	−36 ± 10
	Perpendicular	105 ± 5	25 ± 5	0.24 ± 0.06	2000 ± 10	362 ± 10	−304 ± 10	58 ± 20

hence the highest structural order and magnetic anisotropy. The latter is indicated by the pronounced hard axis out-of-plane in contrast to an easy axis in plane hysteresis loop and a large M_R/M_S value. Due to the coexistence of Ni and NiO in the samples, exchange bias effects are expected.[57] In fact, the hysteresis loops of the samples annealed at 325, 350, and 400 °C whose Ni and NiO interfaces are more predominant, present the highest difference between the positive and negative values of the coercive fields arising due to the exchange bias effect (see Table III). The fact that the magnitude of the exchange bias field is higher for these samples indicates that the Ni and NiO crystallites might have sharp and small-mixed interface areas (as discussed above) enhancing thereby the exchange coupling. For the sample annealed at 700 °C, random signals without the formation of hysteresis are observed when measured either in-plane or out-of-plane, revealing the total consumption of the ferromagnetic Ni.

IV. CONCLUSIONS

The thermal oxidation of nickel thin films depends on AT. The oxidation is detected in all samples by Raman spectroscopy. Annealing also promotes the formation of granular films, as observed by SEM and AFM. The increase of the NiO phase is mediated by the AT. Complete oxidation is obtained at high T of 700 °C or above. XRD reveals that, despite the increase of NiO, the crystallinity of the remaining Ni improves, obtaining the best crystallization after annealing at 350 °C. The presence of Ni and NiO crystallites in the films implies the coexistence of ferromagnetic and antiferromagnetic domains. The magnetic hysteresis loops of the films annealed at 325, 350, and 400 °C reveal exchange bias due to the higher competition between the exchange interactions at the Ni/NiO interfaces compared to the other samples.

ACKNOWLEDGMENTS

The authors acknowledge funding from EPSRC (Nos. RG/63021, EP/K01711X/1, EP/K017144/1, and EP/L016087/1), the FCF of the Universidad Nacional Mayor de San Marcos, the Japan Society for the Promotion of Science, the Collaborative Research Program of the Materials and Structures Laboratory of the Tokyo Institute of Technology, the Leverhulme Trust, a Royal Society Wolfson Research Merit Award, EU Grant CARERAMM and ERC Grant Hetero2D.

[1] *CRC Handbook of Chemistry and Physics*, 93rd ed., edited by W. M. Haynes (CRC, Taylor and Francis Group, FL, 2012).
[2] J. Tersoff and L. M. Falicov, Phys. Rev. B **26**, 6186 (1982).
[3] K. Fueki and J. B. Wagner, J. Electrochem. Soc. **112**, 384 (1965).
[4] J. A. Goebel and F. S. Pettit, Metall. Trans. **1**, 1943 (1970).
[5] H. Gleiter, Acta Mater. **48**, 1(2000).
[6] H. Gleiter, Prog. Mater. Sci. **33**, 223 (1989).
[7] M. E. McHenry and D. E. Laughlin, Acta Mater. **48**, 223(2000).
[8] F. J. Morin, Phys. Rev. **93**, 1199 (1954).
[9] E. Fujii, A. Tomozawa, H. Torii, and R. Takayama, Jpn. J. Appl. Phys., Part 2 **35**, L328 (1996).
[10] D. Adler and J. Feinleib, Phys. Rev. B **2**, 3112 (1970).
[11] E. Antoini, J. Mater. Sci. **27**, 3335 (1992).
[12] G. A. Sawatzky and J. W. Allen, Phys. Rev. Lett. **53**, 2339 (1984).
[13] A. B. Kunz, J. Phys. C: Solid State Phys. **14**, L445 (1981).
[14] H. Sato, T. Mimani, S. Takata, and T. Yamada, Thin Solid Films **236**, 27 (1993).
[15] J. B. Wu, C.-W. Nan, Y. H. Lin, and Y. Deng, Phys. Rev. Lett. **89**, 217601 (2002).
[16] M. J. Carey and A. E. Berkowitz, J. Appl. Phys. **73**, 6892 (1993).
[17] I. Hotovy, J. Huran, and P. Siciliano, Sens. Actuators, B **78**, 126 (2001).
[18] I. M. Chan, T. Y. Hsu, and F. C. Hong, Appl. Phys. Lett. **81**, 1899 (2002).
[19] W. Shin and N. Murayama, Mater. Lett. **45**, 302 (2000).
[20] S. Yamada, T. Yoshioka, M. Miyasita, K. Urabe, and M. Kitao, J. Appl. Phys. **63**, 2116 (1988).
[21] M. Kitao, K. Izawa, K. Urabe, T. Komatsu, S. Kuwano, and S. Yamada, Jpn. J. Appl. Phys., Part 1 **33**, 6656 (1994).
[22] J. F. K. Cooper, *et al.*, J. Appl. Phys. **114**, 083906 (2013).
[23] J. S. E. M. Svensson and C. G. Granqvist, Appl. Phys. Lett. **49**, 1566 (1986).
[24] D. A. Wruck, M. A. Dixon, M. Rubin, and S. N. Bogy, J. Vac. Sci. Technol., A **9**, 2170 (1991).
[25] C. M. Lampert and R. Caron-Popowich, Proc. SPIE **1149**, 56 (1989).
[26] P. Mohanty, C. Rath, P. Mallick, R. Biswal, and N. C. Mishra, Physica B **405**, 2711 (2010).
[27] S. I. Cordoba-Torrsi, C. Gabrielli, A. Hugot-Le Goff, and R. Torresi, J. Electrochem. Soc. **138**, 1548 (1991).
[28] E. Fujii, A. Tomozawa, S. Fujii, H. Torii, H. Torii, M. Hattori, and R. Takayama, Jpn. J. Appl. Phys., Part 2 **32**, L1448 (1993).
[29] J. van Lierop, L. H. Lewis, K. E. Williams, and R. J. Gambino, J. Appl. Phys. **91**, 7233 (2002).
[30] L. Wang, Z. Zhang, and Y. Cao, J. Ceram. Soc. Jpn. **101**, 227 (1993).
[31] L. de los Santos Valladares, *et al.*, Thin Solid Films **520**, 6368 (2012).
[32] L. de los Santos Valladares, *et al.*, Surf. Sci. **603**, 2978 (2009).
[33] L. de los Santos Valladares, A. Bustamante Domínguez, L. León Félix, T. Mitrelias, A. Ionescu, J. Quispe Marcatoma, and C. H. W. Barnes, J. Mater. Sci. Eng. **4**, 1 (2010), available at http://www.davidpublishing.com/show.html?3279.
[34] B. D. Cullity, *Elements of X-ray Diffraction* (Addison-Wesley Publishing Company, Inc., 1956), pp. 96–102.
[35] B. D. Cullity and C. D. Graham, *Introduction to magnetic materials*, 2nd ed. (John Wiley and Sons, Inc., 2009), pp. 48–66 and 115–149.

[36]M. Malathi, "Compact model for a magnetic tunnel junction," Ph.D. thesis (Faculty of Engineering and Technology, SRM University, India, 2009), pp. 40–43.
[37]A. Aharoni, J. Appl. Phys. **83**, 3432 (1998).
[38]A. Aharoni, L. Pust, and M. Kief, J. Appl. Phys. **87**, 6564 (2000).
[39]Powder Diffraction Files PDF-2 of the International Centre for Diffraction Data® (ICDD®), 2001.
[40]D. Tao and F. Wei, Mater. Lett. **58**, 3226 (2004).
[41]L. Wu, Y. Wu, H. Wei, Y. Shi, and C. Hu, Mater. Lett. **58**, 2700 (2004).
[42]I. Hotovy, J. Huran, and L. Spiess, J. Mater. Sci. **39**, 2609 (2004).
[43]T. Okazawa, T. Nishizawa, T. Nishimura, and Y. Kido, Phys. Rev. B **75**, 033413 (2007).
[44]P. A. Temple and C. E. Hathaway, Phys. Rev. B **7**, 3685 (1973).
[45]R. E. Dietz, W. F. Brinkman, A. E. Meixner, and H. J. Guggenheim, Phys. Rev. Lett. **27**, 814 (1971).
[46]R. E. Dietz, G. I. Parisot, and A. E. Meixner, Phys. Rev. B **4**, 2302 (1971).
[47]M. G. Cottam and D. J. Lockwood, *Light Scattering in Magnetic Solids* (Wiley, New York, 1986).
[48]P. A. Fleury and R. Loudon, Phys. Rev. **166**, 514 (1968).
[49]N. Mironova-Ulmane, A. Kuzmin, I. Steins, J. Grabis, I. Sildos, and M. Pars, J. Phys.: Conf. Ser. **93**, 012039 (2007).
[50]W. Duan, S. H. Lu, Z. L. Wu, and Y. S. Wang, J. Phys. Chem. C **116**, 26043 (2012).
[51]M. R. Pinnel, H. G. Tompkis, and D. E. Heath, J. Electrochem. Soc. **126**, 1274 (1979).
[52]S. Veena Kumari, M. Natarajan, V. K. Vaidyan, and P. Koshy, J. Mater. Sci. Lett. **11**, 761 (1992).
[53]N. Cabrera and N. F. Mot, Rep. Prog. Phys. **12**, 163 (1949).
[54]A. Atkinson and R. I. Taylor, J. Phys. Chem. Solids **47**, 315 (1986).
[55]X. Wu, C. Ossadnik, C. Eggs, S. Veprek, and F. Phillipp, J. Vac. Sci. Technol., B **20**, 1368 (2002).
[56]S. Andersson and L. Dzhavadov, J. Phys.: Condens. Matter **4**, 6209 (1992).
[57]J. Nogués and I. K. Schuller, J. Magn. Magn. Mater. **192**, 203 (1999).